ANALYSIS OF ORBIT STABILITY IN THE GEOSYNCHRONOUS REGION FOR END-OF-LIFE DISPOSAL

Camilla Colombo [(1)], Ioannis Gkolias [(2)]

[(1)] *Politecnico di Milano, Department of Aerospace Science and Technology, via La Masa 34, 20156 Milan, Italy, Email: camilla.colombo@polimi.it*
[(2)] *Politecnico di Milano, Department of Aerospace Science and Technology, via La Masa 34, 20156 Milan, Italy, Email: ioannis.gkolias@polimi.it*

ABSTRACT

This paper characterises the dynamical structure and long term stability of the geostationary orbit region, including inclined orbits. Long-term orbit propagation through semi-analytical techniques is employed to identify the effect of gravitational luni-solar and solar radiation pressure perturbations and their coupling with the Earth's oblateness and triaxiality. Maps showing the amplitude of the oscillation of the orbital parameters are produced as the results of these long-term simulations over an extended grid of initial orbit conditions. These maps will be used to design manoeuvres for fuel efficiency transfer to stable graveyard orbits or re-entry "highways".

Keywords: Geostationary orbit, long-term evolution, disposal, graveyard, space debris, ReDSHIFT.

1 INTRODUCTION

Spacecraft in Geostationary orbit (GEO) represent a fundamental aspects of space activities and services to the Earth. According to the publicly-available two-line element sets around 1200 total objects are catalogued at a semi major axis around the geostationary value, including active spacecraft, rocket bodies and space debris. Apart of selecting safe procedures for operational spacecraft such as orbits with fewer debris, specific altitude configurations, or implementing active collision avoidance manoeuvres, space debris guidelines aim at limiting the creation of new debris (by prevention of in-orbit explosions) and implementing end-of-life disposal manoeuvres to free the GEO protected region. At altitudes below 600 kilometres, orbital debris will re-enter within a few years due to atmospheric drag. Intervention to remove and prevent further creation of debris above that altitudes should therefore be the primary focus of passive mitigation measures. The European Space Agency (ESA) "Requirements on Space Debris Mitigation for ESA Projects" [1] set the following Operational Requirements (OR) for disposal of GEO spacecraft.

OR-02. Space systems operating in the GEO protected region shall be disposed by permanently removing them from the GEO protected region. Conformance with the GEO disposal requirement can be ensured by using a disposal orbit with the following characteristics:

- eccentricity ≤ 0.005,
- minimum perigee altitude Δh_p above the geostationary altitude according to

$$\Delta h_p \geq 235 + 1000\, c_R\, A/m$$

where h_p is in km, c_R is the solar radiation pressure coefficient of the space system at the beginning of its life (0 for completely transparent material, 1 for completely absorbing material, 2 for totally reflecting material), A/m is the cross-section area (in m^2) to dry mass (in kg) of the space system.

OR-03. Where practicable and economically feasible, space systems outside the low Earth orbit (LEO) and GEO protected regions shall implement means of end-of-life orbit disposal to avoid long-term interference with operational orbit regions, such as the Galileo orbit. The geosynchronous protected region (GEO region) is a segment of a spherical shell defined by [1]:

- lower altitude boundary = geostationary altitude minus 200 km,
- upper altitude boundary = geostationary altitude plus 200 km,
- latitude sector: 15 degrees South $\leq$ latitude $\leq$ 15 degrees North,
- geostationary altitude $h_{GEO} = 35786$ km

It is in the common interest of space agencies and satellite operators to collaborate for this region to remain clear for future missions. End-of-life disposal manoeuvres for GEO satellites not only allow the orbit to be reused in the future but keep in control the space debris population especially within the protected region. Mitigation strategies employing a higher altitude orbit (super-synchronous) orbit as a graveyard, were one of the first proposed solutions [2]. For the years to come, this solution was adopted as the main strategy for GEO satellites since it provides a significant reduction in the collision risk at the cost of a couple of months of operational lifetime. The stability of the super-synchronous graveyard has become the topic of many studies [3, 4, 5], which confirmed that, indeed, an eccentricity of 0.005 and a disposal perigee 300 km

above GEO, reassure no future interaction with the protected region. Further studies revealed that the direction of the eccentricity vector at the time of disposal also affects the long-term evolution of graveyard orbits. Pointing the initial perigee towards the Sun can reduce the long-term perigee variations and therefore diminish the risk of interference with the protected region [6, 7, 8]. The sun-pointing perigee strategy is also easy to adopt, since GEO satellites have a similar behaviour during their operational lifetime.

Another interesting aspect of the GEO dynamics is the exploitation of the natural lunisolar perturbations. Nowadays, only a small portion of the GEO satellites exploit the stable plane of about 7.3 degrees inclination in order to avoid the fuel-expensive, North-South station-keeping [9, 10]. The exploitation of this idea in designing graveyard orbits is not so practical since inclination manoeuvres are quite expensive. Finally, the discovery of high area-to-mass debris in eccentric orbits around the GEO region [11] renewed the interest in the stability of graveyard orbits [12]. It appears that the satellites in the geostationary and super-synchronous graveyard are producing a population of high area-to-mass debris that cannot be contained by the low-eccentricity, low-inclination super-synchronous graveyard and can potentially cross the protected region, causing damage to operational spacecraft. A generalised stable plane, that could contain the high area-over-mass debris has been proposed [13], however it shares the same difficulties in disposal orbit design as the classical plane. All the above discussion suggests that designing a GEO disposal orbit is not so trivial and single equation guidelines are inadequate. Therefore, an optimised disposal manoeuvre should be considered for each particular case, considering the operational orbit of the satellite, the epoch of the disposal, the remaining fuel, the possibility to create high area-over-mass debris and many other factors.

With this as our final goal, this paper characterises the dynamical structure and long term stability of the circumterrestrial space at the geostationary altitude, including inclined Geosynchronous Orbit such as the one of the BeiDou constellation [14, 15]. Long-term orbit propagation through semi-analytical techniques and numerical high fidelity models is employed to identify the effect of gravitational luni-solar and Solar Radiation Pressure (SRP) perturbations and their coupling with the Earth's oblateness and triaxiality. Maps of the amplitude of the oscillation in orbital parameters are produced as the results of these long-term simulations over an extended grid of initial orbit conditions. These maps will built the basis for an analysis of the characteristic frequencies of the perturbation effects and will be used to design manoeuvres for fuel efficiency transfer to stable graveyard orbits or re-entry "highways". The present study is part of a joint effort with the groups of IFAC-CNR, (Italy) and Aristotle University of Thessaloniki (Greece) that are studying the low Earth orbit [16] and the Medium Earth orbit [17] regions in the framework of the Revolutionary Design of Spacecraft through Holistic Integration of Future Technologies (ReDSHIFT) project.

2 OBJECT DISTRIBUTION IN GEO

The MASTER 2013 space debris population of objects with characteristic length larger than or equal to 10 cm and the Union of Concerned Scientist (UCS) database [18] were analysed to obtain a snapshot of the current use of space (see Figure 1). The spatial density of the GEO population is several orders of magnitude below that of the LEO population, and the resultant collision probabilities are therefore lower. However, no natural mechanism like atmospheric drag exists in the geostationary ring, to limit the lifetimes of debris at this altitude. Figure 2 shows the distribution of total objects in GEO, where the colour bars represent the numbered of objects per bin for the semi-major axis, eccentricity, and inclination phase space. The distribution of *A/m* ratios for GEO objects is shown in Figure 3.

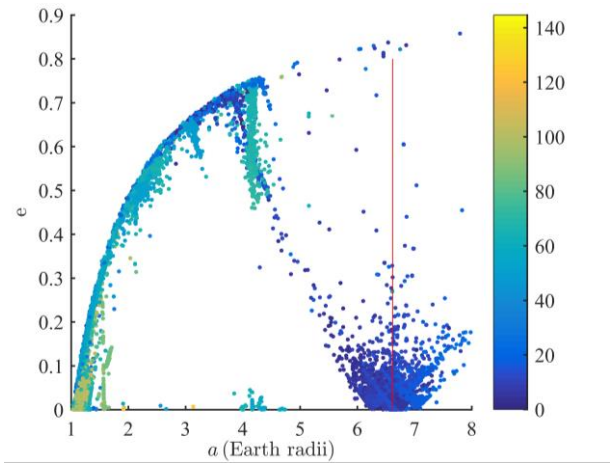

a)

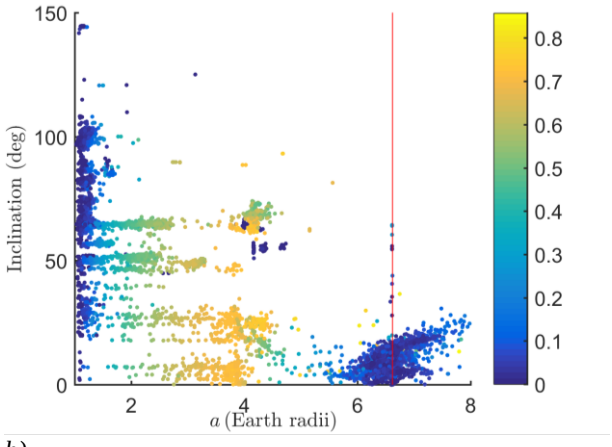

b)

Figure 1. Distribution of space objects from LEO to GEO in a) Semi-major axis and eccentricity and b) semi-major axis and inclination.

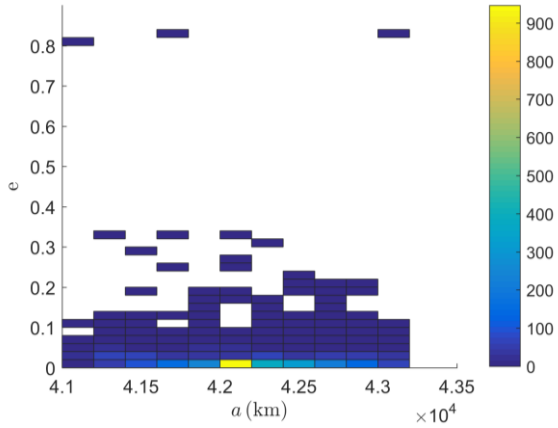

a)

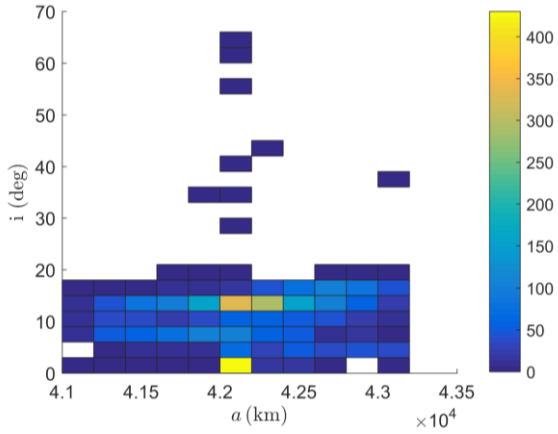

b)

Figure 2. Total objects distribution across the GEO ring in a) Semi-major axis and eccentricity and b) semi-major axis and inclination. Bin number = [11; 42] (optimised).

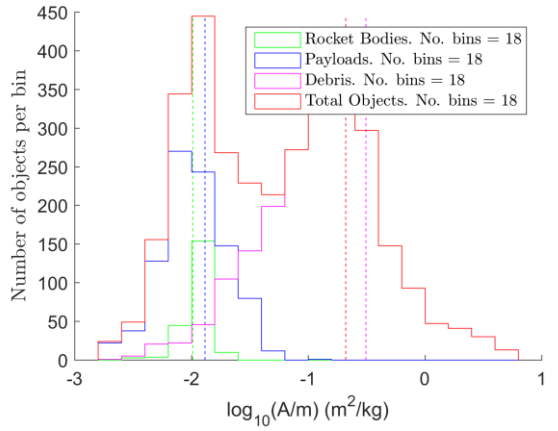

Figure 3. Area-to-mass distribution across the GEO ring.

For the long term analysis of the GEO phase space a reference value of the area-to-mass ratio is required. Two cases have been analysed: a standard value, typical of satellites, and a case where the effect of SRP is enhanced. The SRP-augmented case is representative on which behaviour could be expected in the case of a high-area-to-mass fragment, deriving from explosions or collisions in orbit or the natural deterioration of spacecraft structures, or in the case a spacecraft is equipped with a SRP-augmenting device (e.g., large solar sail) deployed at the end-of-life to favour the end-of-life disposal [19].

For the standard case, a value of $c_R\, A/m = 0.012$ m^2/kg was considered, while for the SRP-augmented case an indicative value of $c_R\, A/m = 1$ m^2/kg was selected instead. Table 1 contains the average and the standard deviation of the A/m distribution in GEO according to MASTER 2013.

Table 1. Area-to-mass ratios for the debris population.

Object type	**Average *A/m* [m^2/kg]**	**Standard deviation**
Population	0.210	0.005
Satellites	0.013	0.010
Rocket bodies	0.010	0.002

3 ORBIT MODEL: PLANETARY ORBITAL DYNAMICS (PLANODYN)

The Planetary Orbital Dynamics (PlanODyn) suite was originally designed for the analysis of highly elliptical orbit disposal manoeuvres by enhancing the effects of natural perturbations [20, 21], then extended to treat also low and medium and geostationary Earth orbits. The orbit propagator within PlanODyn implements the single and double averaged dynamics of the Lagrange or Gauss planetary equations written in orbital elements. It also allows the analytical estimation of the Jacobian matrix to be used for calculating the state transition matrix for sensitivity analysis, stability studies and uncertainty propagation.

PlanODyn propagates the Earth-centred dynamics by means of the averaged variation of the disturbing potential or acceleration [20]. For the single average approach, the averaging is performed over the orbit revolution of the spacecraft around the central body, for the double average approach the averaging is the also performed over the revolution of the perturbing body around the central body. The averaged equations are integrated with an explicit Runge-Kutta (4, 5) method, with Dormand-Prince pair [22] or with a variable-step, variable-order Adams-Bashforth-Moulton solver of orders 1 to 12. [23]. The perturbations implemented in PlanODyn are: zonal and tesseral harmonics of the Earth's gravity potential, third-body perturbations, solar radiation pressure and atmospheric drag. For the gravitational perturbing effect of the Moon and the Sun, the third body potential is expanded in series of a/a_{3B} where a and a_{3B} are the semi-major axis of the spacecraft and the third body respectively. The disturbing

potential is expanded up to order 5 in the Legendre polynomial. For the Earth's gravity model, different harmonics models can be selected. For this work, several tests were performed to identify the *minimum* gravity model to be used for the GEO region (a J_2-only model, a zonal model up to degree 6, a 2 × 2 model, and a 5 × 5 model). For the non-axisymmetric gravity field model, the recursive formulation by Cunningham is implemented [24]. In future work an average approach will be used. Different ephemerides models are available, in this work the JPL ephemerides implemented in the SPICE toolkit are used. The complete structure of PlanODyn is summarised in Figure 4.

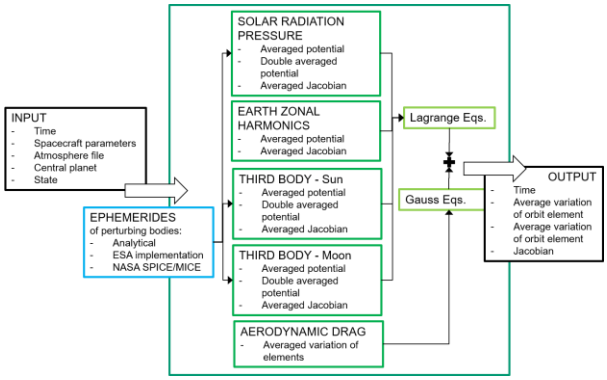

Figure 4. PlanODyn dynamics schematics.

Figure 5 shows an example result of the validation performed between the orbit propagation through PlanODyn and the integration obtained through a full dynamics code (HiFiODyn), which implements the perturbing accelerations and simulates the dynamics in terms of the Gauss perturbation equations. The initial orbit considered in the example is characterised by semi-major axis, $a = a_{GEO}$, eccentricity, $e = 0.001$, inclination, $i = 0.1\,\text{deg}$, Right Ascension of the Ascending Node (RAAN), $\Omega = 0\,\text{deg}$, anomaly of perigee, $\omega = 0\,\text{deg}$ and mean anomaly, $M = 0\,\text{deg}$ with $c_R\, A/m = 0.01\,\text{m}^2/\text{kg}$. The orbit is propagated from 2020/06/21.28 for a period of 30 years. As it can be seen, the PlanODyn formulation replicates the orbital element evolution of the non-averaged formulation, particularly in semi-major axis, inclination, and right ascension of the ascending node. The long-term trends in eccentricity and perigee argument are also well represented. Note that this is likely the most stringent test, as this is an almost circular, equatorial orbit. For a slightly larger initial eccentricity, the two codes would be a perfect match.

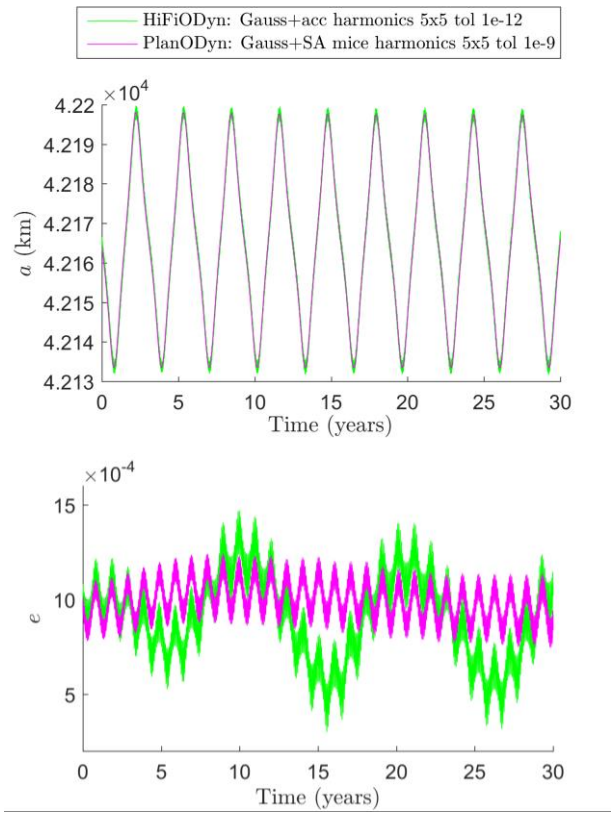

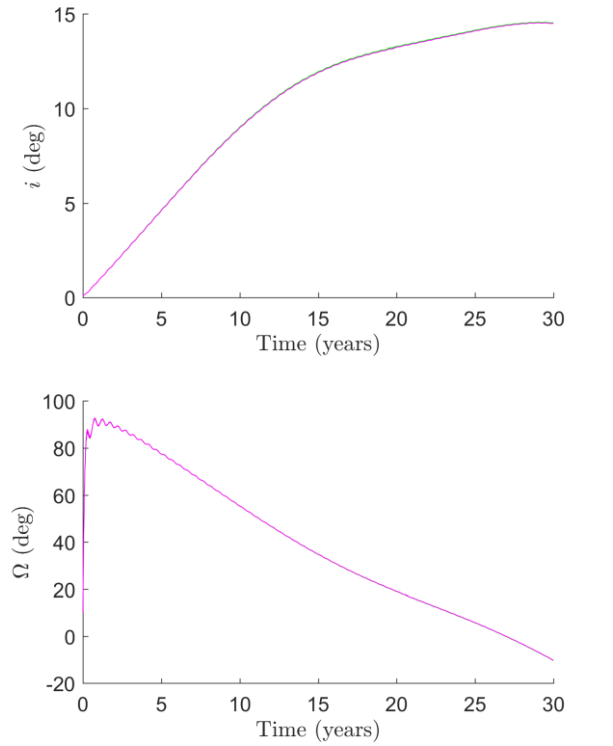

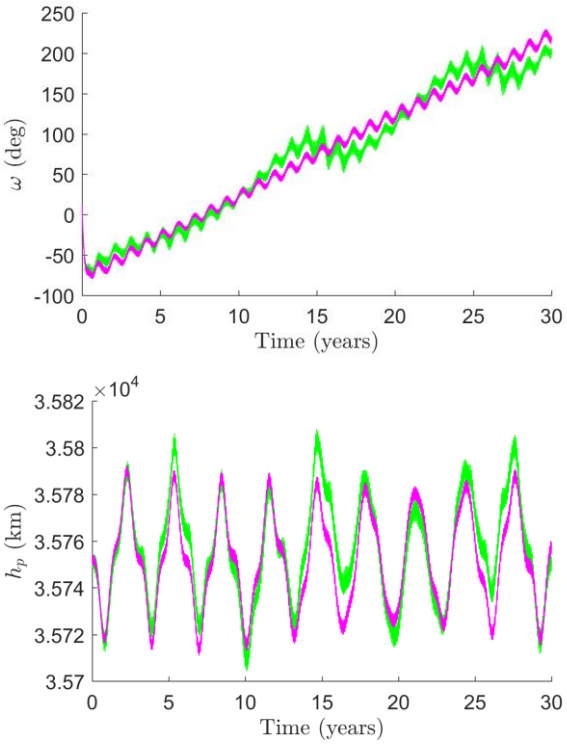

Figure 5. Comparison of PlanODyn with non-averaged dynamics for a typical geosynchronous orbit.

4 LONG TERM EVOLUTION DYNAMICS

As it was previously proposed in [25, 26], to the purpose of studying the long term evolution of many initial conditions, a grid approach is here adopted. A grid is defined in the domain of semi-major axis, inclination, eccentricity, right ascension of the ascending node and anomaly of the perigee. For each initial condition on the grid the orbit evolution is calculated over a period of 30 or 120 years with PlanODyn, using the single averaged dynamics, to get the time variation of the orbital elements. From the time vector evolution the variation of the eccentricity, semi-major axis and inclinations are computed as:

$$\Delta e = \max_t e(t) - \min_t e(t) \quad t \in [t_0 \quad t_0 + \Delta t]$$
$$\Delta i = \max_t i(t) - \min_t i(t) \quad t \in [t_0 \quad t_0 + \Delta t]$$
$$\Delta a = \max_t a(t) - \min_t a(t) \quad t \in [t_0 \quad t_0 + \Delta t]$$

and stored in matrices with the same dimension as the grid of initial conditions. As shown in [20] the variation of the orbital elements can be used as a measure of their oscillation due to the effect of perturbations. The objective of this phase space analysis is to accurately map the phase space associated the eccentricity vector to identify the regular and chaotic zones.

The grid analysed for GEO consisted of a semi-major axis range of [−500; +500] km, with respect to the geosynchronous semi-major axis of a_{GEO} = 42164.17 km, an eccentricity range of [0; 0.3], and an inclination range of [0; 5] degrees (see Table 2). The initial values of Ω and ω were set with respect to the Earth-Moon plane and were then converted into the Earth-centred equatorial system, where the simulations were performed. Four different values of $\Delta\Omega = \Omega - \Omega_{Moon}$ were chosen to describe the node of the orbit with respect to the lunar node (both with respect to the Earth-centred equatorial J2000 reference frame); namely $\Delta\Omega$ of 0, 90, 180, 270 degrees and seven different values of ω_{Moon} = {0; 30; 60; 90; 120; 150; 180} degrees, measured from the ascending node of the satellite orbit with respect to the Earth-Moon plane.

A second grid with an extended range of eccentricity (up to 0.9) and inclination (up to 90 degrees), for the same set of values of *a*, was also studied (see Table 3). To analyse the effect of the C_{22} gravitational harmonics, different initial condition of the satellite in terms of the resonant angle were considered. Both a "nominal" and an "enhanced" SRP case was examined, corresponding to $c_R A/m$ = 0.012 m²/kg or 1 m²/kg. A common starting epoch t_0 for the simulation is selected, which influences on the position of the Moon and the Sun. Two initial starting dates are chosen, one close to the winter solstice of 2018, and the other close to the summer solstice of 2020; at solstices the projection on the ecliptic of the spin axis of the Earth lies on the Earth-Sun line, and at the two dates we chose also the Moon happens to be close to that line (on the same side as the Sun in 2020, on the opposite side in 2018). In the summer solstice of 2020 also the line of nodes of the lunar orbit is aligned with the Earth-Sun line, and in fact a solar eclipse occurs; in the winter solstice of 2018 there is no eclipse, just a Full Moon. Table 2 and Table 3 summarise the breakdown of the initial conditions of the detailed simulations performed for the GEO region.

Table 2. Grid definition for the GEO region study.

Parameters	Values
Δa [km]	{−500;−250;−200;−150;−10;−70;−40;−20; 0; 20; 40; 70; 100; 150; 200; 250; 500}
e	{0; 0.001; 0.01; 0.03; 0.05; 0.075; 0.1; 0.125; 0.15; 0.175; 0.2; 0.25; 0.3}
i [degrees]	{0; 0.001; 1:1:5}
$\Delta\Omega_{Moon}$ [degrees]	{0; 90; 180; 270}
ω_{Moon} [degrees]	{0; 30; 60; 90; 120; 150; 180}

Table 3. Extended grid definition for the GEO region study.

Parameters	Values
Δa [km]	{−500;−250;−200;−150;−10;−70;−40;−20; 0; 20; 40; 70; 100; 150; 200; 250; 500}
e	{0.35 : 0.05: 0.9}
i [degrees]	{0.001; 1:1:5; 6:2:20; 25:5:90}
$\Delta\Omega_{\text{Moon}}$ [degrees]	{0; 90; 180; 270}
ω_{Moon} [degrees]	{0; 30; 60; 90; 120; 150; 180}

5 DETAILED DYNAMICAL GEO MAPS

As it can be seen in the figures in Section 1, the satellites in the GEO region are concentrated around the geostationary radius and with an eccentricity range of [0 – 0.3] and inclination range of [0 − 70] degrees with the highest satellite around the zero-eccentricity and zero-inclination band (e within [0 – 0.3] and i within [0 − 5] degrees). Therefore, a finer grid was run around these values according to the grid in Table 1. The next section will present the results of the long-term evolution maps considering the case of a conventional GEO spacecraft (i.e. $c_R A/m = 0.012$ m^2/kg) and the SRP-augmented case (i.e. $c_R A/m = 1$ m^2/kg). The results shown in this paper are for the first starting epoch.

5.1 CONVENTIONAL SPACECRAFT

5.1.1 Effect of the Earth's triaxiality

The stable and unstable equilibria caused by the Earth's triaxiality, and the associated librational and rotational solutions, can be appreciated by propagating an initial GEO orbit for different starting values of the resonant angle defined as:

$$\lambda = \Omega + \omega + M$$

Figure 6 depicts for an initial orbit with semi-major axis as the GEO radius the change in semi-major axis Δa in km over 30 years as function of the initial orbit's eccentricity and ω_{Moon} for two different starting values of the mean anomaly. Note that the Δa does not depend on the initial inclination of the orbit (i.e., the same figure was be obtained for any inclination tested in the range [0 − 5] deg).

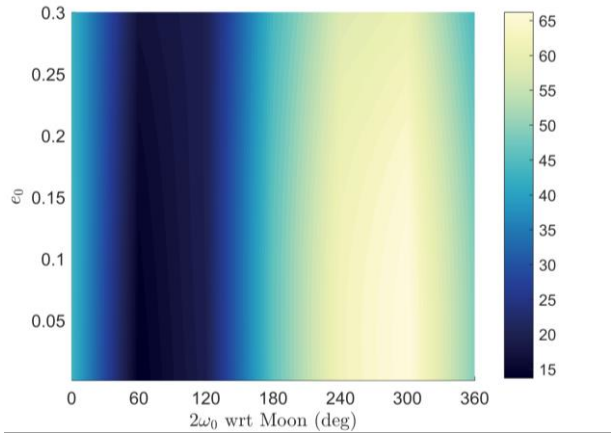

(a) M_0 = 30 degrees.

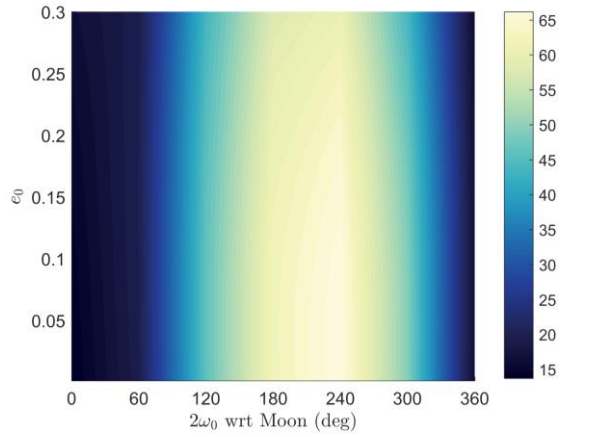

(b) M_0 = 60 degrees.

Figure 6. Maximum variation of Δa over 30 years for initial orbit with $a = r_{\text{GEO}}$, $\Omega_0 = 0$, initial eccentricity between [0−0.3] and inclination of inclination range of [0 − 5] degrees, satellite with $c_R A/m = 0.012$ m^2/kg.

If we now compute the change in semi-major axis Δa still over 30 years considering initial conditions distributed over a grid of semi-major axis (steps of 5 km) and λ angle (obtained by discretising the initial Ω with a step of 18 deg, keeping the initial ω and M fixed to 0), we obtain the plot in Figure 7, where the colour bar is the variation of semi-major axis in km. The stable and unstable longitudes due to the Earth's triaxiality are clearly visible. Note that this plot shows the stable and the unstable longitude (equilibrium, librational or rotational solutions), but is not a measure of the orbit stability.

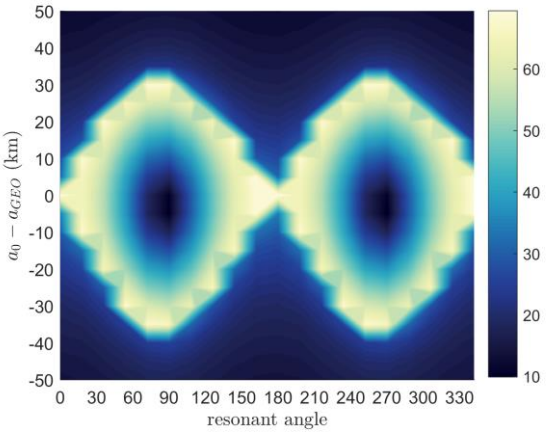

Figure 7. Maximum variation of Δa over 30 years for initial orbit with $a = r_{\text{GEO}} + [-50, 50]\, km$, $e_0 = 0.01$, $i_0 = 0\, deg$, $\Omega_0 = 0$, $\omega_0 = 0\, deg$ and $\lambda = [0, 360]\, deg$, satellite with $c_R\, A/m = 0.012\ m^2/kg$.

5.1.2 Effect of the luni-solar perturbations

The effect of the luni-solar gravitational perturbation can be seen in eccentricity-ω_{Moon} maps as in [20] for analysing the Lidov-Kozai mechanism in highly elliptical orbits. Figure 8 shows the variation of eccentricity Δe over 30-year propagation for an initial orbit with $a = r_{\text{GEO}}$ and $\Delta\Omega = \Omega - \Omega_{\text{Moon}} = 0$ degrees. For low inclinations (Figure 8a – Figure 8g) the effect of luni-solar perturbations causes bounded oscillations in eccentricity, which depend on the initial ω with respect to the Moon's plane $\omega_{\text{Moon},0}$. The maximum of the eccentricity variation is achieved for $2\omega_{\text{Moon},0} \simeq 180$ and 0 degrees, and it is accentuated for larger initial eccentricity. The dynamics become more interesting for higher inclinations (Figure 8h – Figure 8v), where the Lidov-Kozai loops clearly appear [27].

When also the initial semi-major axis is varied we can analyse the long-term behaviour of orbits with different initial eccentricity and $\omega_{\text{Moon},0}$ with respect to the Earth-Moon plane by calculating for each orbit evolution the maximum and minimum Δe achieved over the 30 year-period and plotting on the grid of initial orbit semi-major axis and inclination grid the maximum and minimum Δe that the orbit can get over its evolution by changing e_0 and $\omega_{\text{Moon},0}$

$$\Delta e_{\max} = \max_{e_0,\, \omega_{\text{Moon},0}} \Delta e,$$

$$\Delta e_{\min} = \min_{e_0,\, \omega_{\text{Moon},0}} \Delta e$$

The results is presented in Figure 9. Note that the choice of the representation of the anomaly of the perigee with respect to the Moon's plane, makes the problem independent from the choice of $\Delta\Omega$ as can be seen in Figure 9b and d. This corresponds to the elimination of nodes [27, 20].

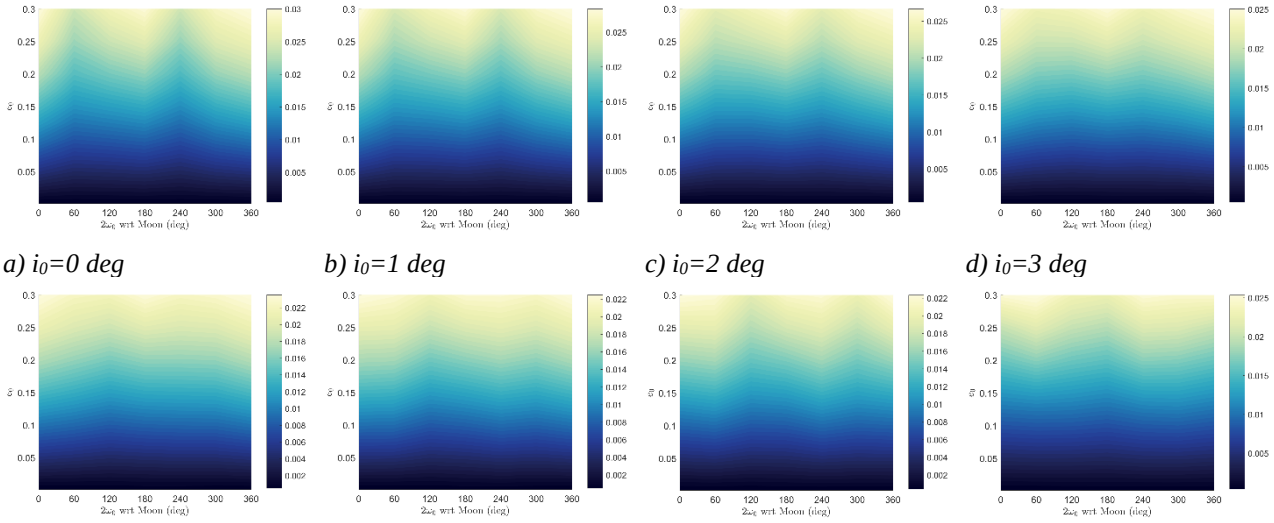

a) i_0=0 deg *b) i_0=1 deg* *c) i_0=2 deg* *d) i_0=3 deg*

e) i_0=4 deg *f) i_0=5 deg* *g) i_0=6 deg* *h) i_0=10 deg*

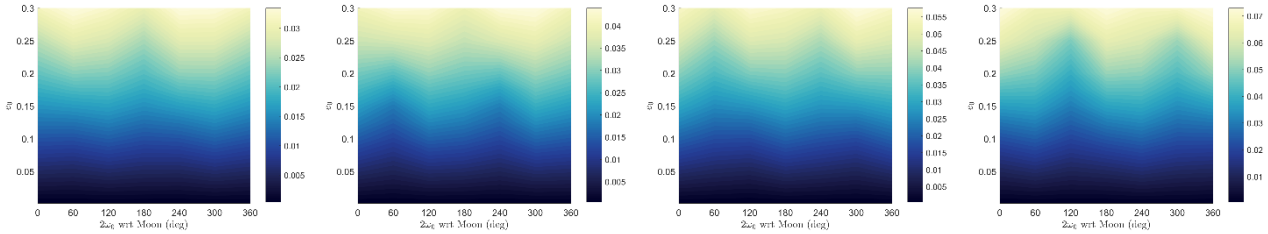

i) i_0=15 deg *l) i_0=20 deg* *m) i_0=25 deg* *n) i_0=30 deg*

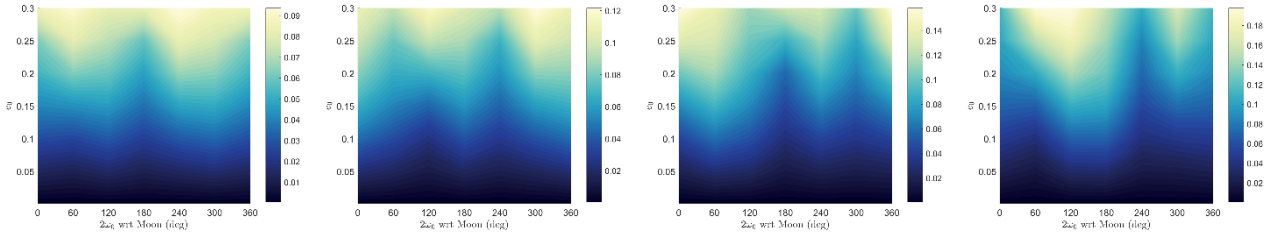

o) i_0=35 deg *p) i_0=40 deg* *q) i_0=45 deg* *r) i_0=50 deg*

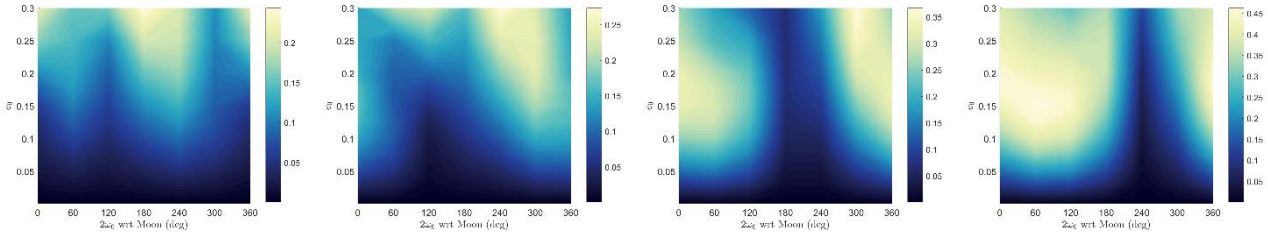

s) i_0=55 deg *t) i_0=60 deg* *u) i_0=65 deg* *v) i_0=70 deg*

Figure 8. Maximum variation $\Delta e_{\max}$ over 30 years for initial orbit with $a = r_{\text{GEO}}$, $\Omega_0 = 0$, initial eccentricity between [0−0.3] and inclination of inclination range of [0 − 70] degrees, satellite with $c_R\, A/m = 0.012$ m^2/kg.

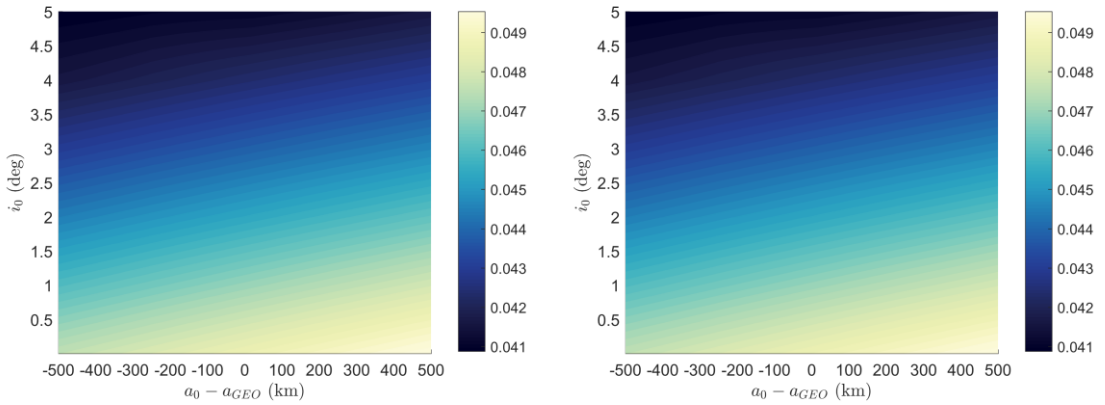

a) $\Delta e_{\max}$, $\Delta\Omega = 0$ deg. *b)* $\Delta e_{\max}$, $\Delta\Omega = 90$ deg

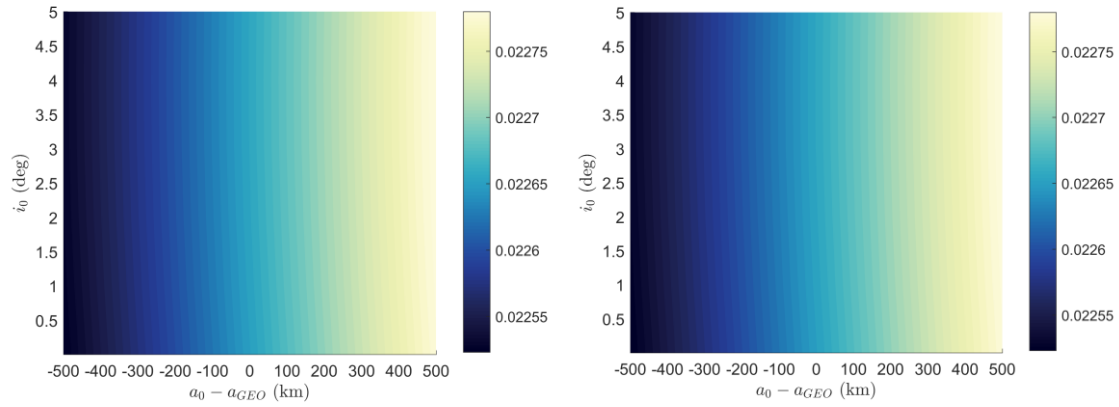

c) $\Delta e_{\min}$, $\Delta\Omega = 0$ deg. *d)* $\Delta e_{\min}$, $\Delta\Omega = 90$ deg

Figure 9. Maximum (a) and minimum (b) variation Δe *over 30 years for initial orbit with* $a = r_{\text{GEO}} + [-500, +500]$ *km, initial eccentricity between [0−0.3] and inclination of range of [0 − 5] degrees, satellite with* $c_R\, A/m = 0.012$ m^2/kg.

Now fixing the initial eccentricity to two set values of 0.01 and 0.1 and the initial RAAN and anomaly of the perigee to 0, the orbit propagation is calculated over 120 years for many initial conditions in *a* and *i* we can store the maximum eccentricity that the orbit will attain over the 120-year evolution. The result is shown in Figure 10. While for low inclination the variation of eccentricities are limited, for initial inclinations higher than 55 degrees the maximum eccentricity is very high. This leads to natural re-entry for the initial conditions represented by a light yellow colour in Figure 10, as for those cases the maximum eccentricity reaches the critical eccentricity for re-entry:

$$e_{\text{crit}} = 1 - \left(R_{\text{E}} + 120\,\text{km}\right)/r_{\text{GEO}} = 0.8461$$

Therefore, Figure 10 gives as a measure of the orbit stability. For low-inclinations natural re-entry solutions are not found, but for high inclinations, for example around the inclination of the BeiDou system [14, 15] (*i* = 56 degrees), natural re-entry is possible over a period of around 120 years. For low inclination conventional GEO, the useful information contained on these maps is the magnitude (and time-scale) of eccentricity variations, for each initial condition. This is what is needed in order to define the optimal graveyard disposal solution. Another parameter interesting for the selection of the graveyard orbit is the variation of orbit inclination over the 120-year time period. As it can been seen in Figure 11, the Laplace plane in the band of 5-15 degrees is visible, where the variation of eccentricity is limited. This plane would be the one where the long term oscillation of the inclination is bounded. If in addition the perigee vector is placed as pointing toward the Sun-direction and the eccentricity is chosen as a frozen orbit, the orbit will present also low oscillations in eccentricity.

As an example three trajectories (evolution of eccentricity and inclination) are shown in Figure 12. They correspond to one initial condition close to the Laplace plane with initial inclination of 8 degrees, one initial condition close to the GEO graveyard orbit with initial inclination of 0 degrees, and one initial condition with inclination of 68 degrees that achieves re-entry in less than 120 years.

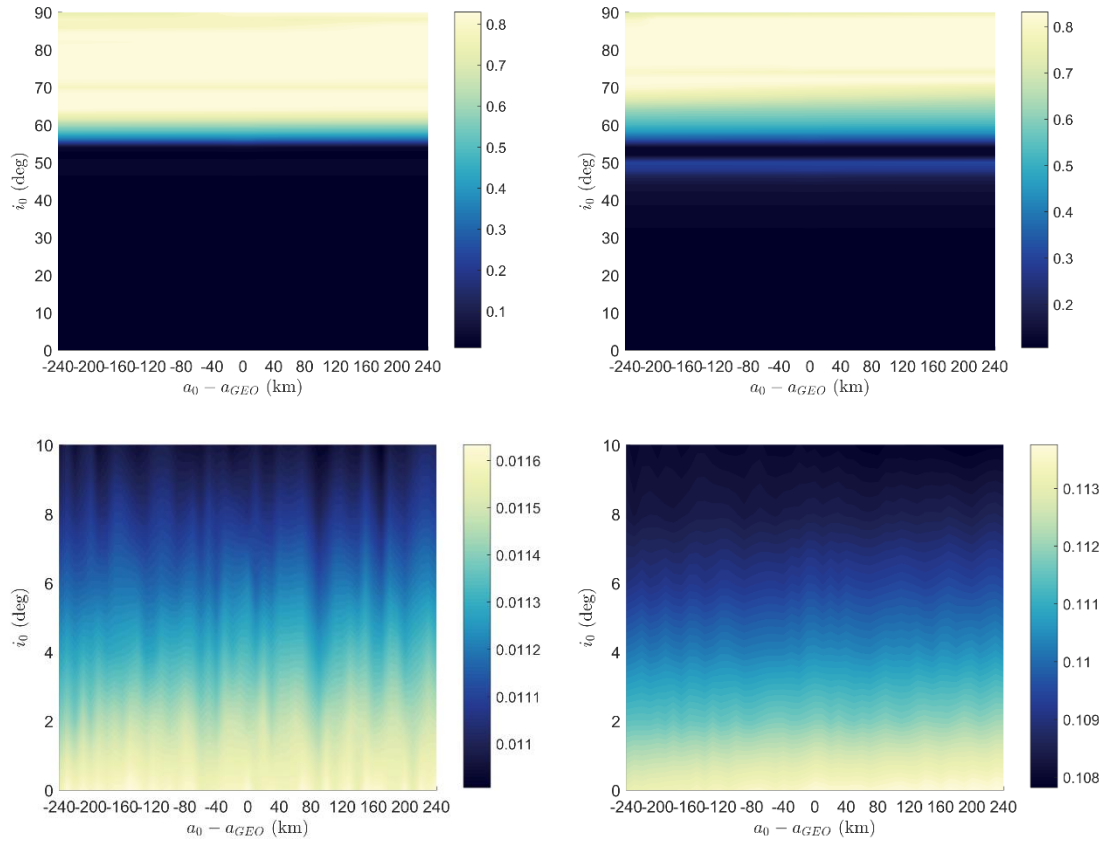

a) $e_0 = 0.01$ *b)* $e_0 = 0.1$

Figure 10. Maximum eccentricity attained over 120 years for initial orbit with $a = r_{\text{GEO}} + [-240, +240]$ *km, initial eccentricity of (a) 0.01 and (b) 0.1, inclination of range of [0 − 90] deg, initial RAAN and anomaly of the perigee of 0 deg. Satellite with* $c_R\, A/m = 0.012$ m^2/kg.

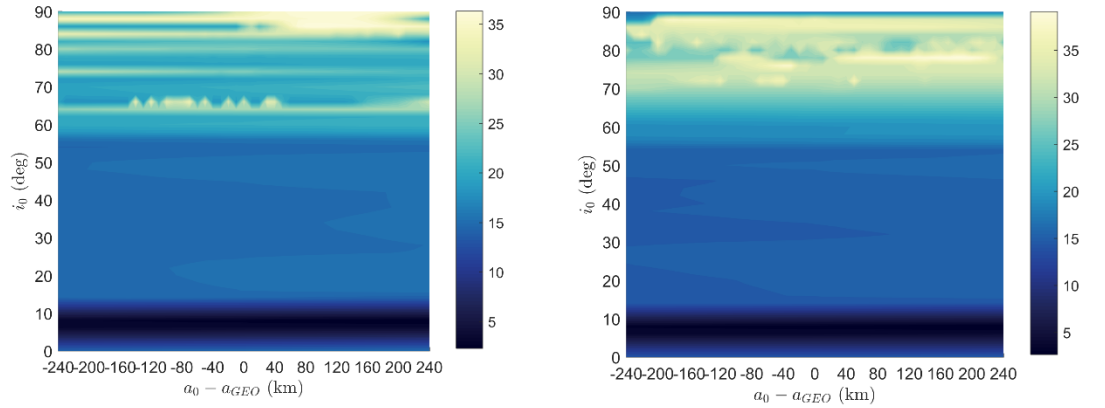

a) $e_0 = 0.01$. *b)* $e_0 = 0.1$.

Figure 11. Variation of inclination Δi *in degrees over 120 years for initial orbit with* $a = r_{\text{GEO}} + [-240, +240]$ *km, initial eccentricity of (a) 0.01 and (b) 0.1, inclination of range of [0 − 90] deg, initial RAAN and anomaly of the perigee of 0 deg. Satellite with* $c_R\, A/m = 0.012$ m^2/kg.

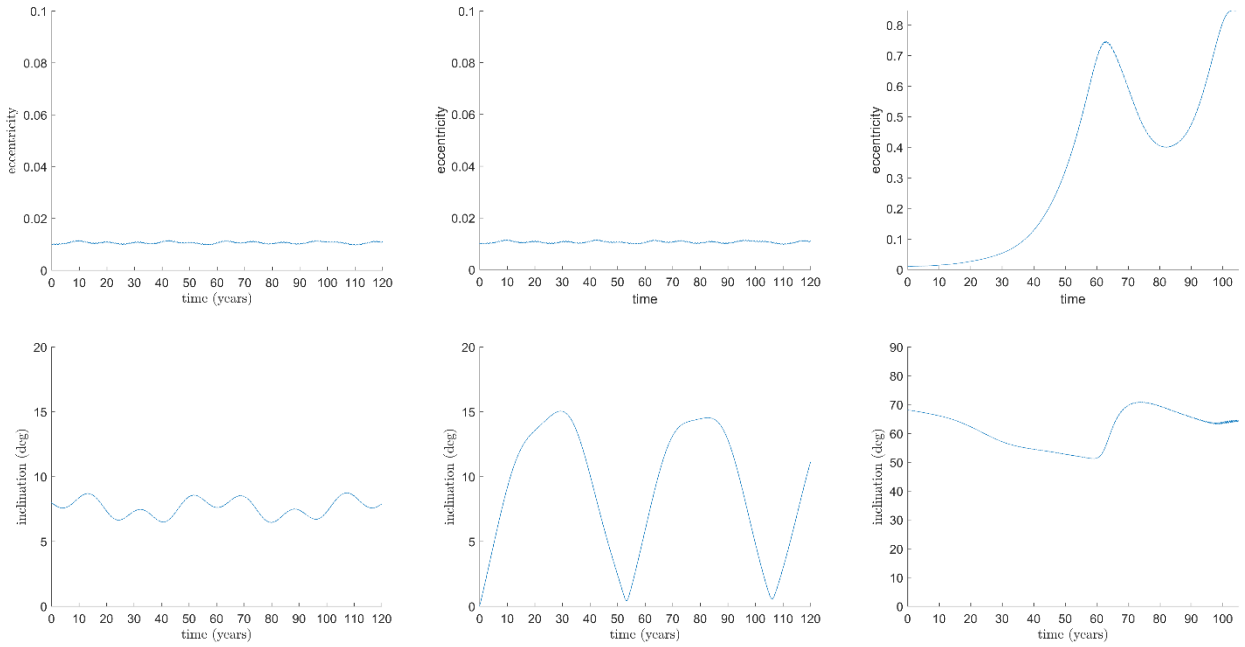

a) Close to Laplace plane. *b) Graveyard.* *c) Re-entry.*

Figure 12. Orbit evolution for three initial conditions (all with Ω_0=0, ω_0=0). A) Initial condition close to the Laplace plane: e_0=0.01, a_0=r_{GEO}+240 km, i_0=8 deg. B) Graveyard orbit: e_0=0.01 a_0=r_{GEO}+240 km, i_0=0 deg. C) Re-entry orbit: e_0 =0.01, a_0=r_{GEO}–200 km, i_0=68 deg.

5.2 AUGMENTED-SRP CASE

The effect of eccentricity and inclination oscillations induced by luni-solar perturbations is enhanced by the effect of solar radiation pressure. Indeed, the effect of SRP causes long term libration of the eccentricity vector around the direction Earth-Sun [28]. The SRP effect can be seen the example in Figure 13 where $c_R\, A/m = 1$ m^2/kg. Figure 13, as Figure 8, shows the variation of eccentricity Δe over 30-year propagation for an initial orbit with $a = r_{GEO}$ and $\Delta\Omega = \Omega - \Omega_{Moon,0} = 0$ degrees. With respect to Figure 8, here the variation of eccentricity is more pronounced; for high initial inclinations the Lidov-Kozai loops clearly appear [27].

The behaviours shows very small differences as the initial semi-major axis of the orbit is modified within the GEO protected region. Figure 14 represents the same maps as Figure 13 but with a fixed initial inclination equal to 70 degrees and varying the semi major axis of −500, −200, 200 and 500 km, respectively.

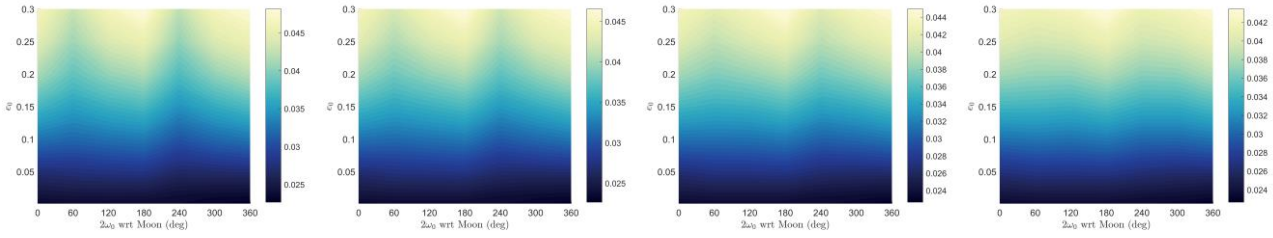

a) i_0=0 deg *b) i_0=1 deg* *c) i_0=2 deg* *d) i_0=3 deg*

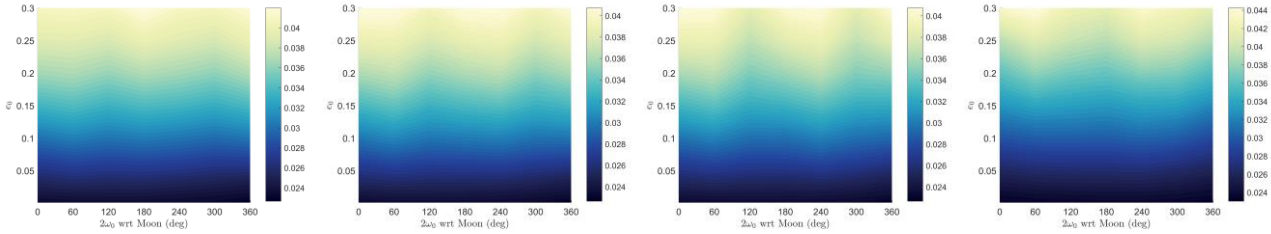

e) i_0=4 deg *f) i_0=5 deg* *g) i_0=6 deg* *h) i_0=10 deg*

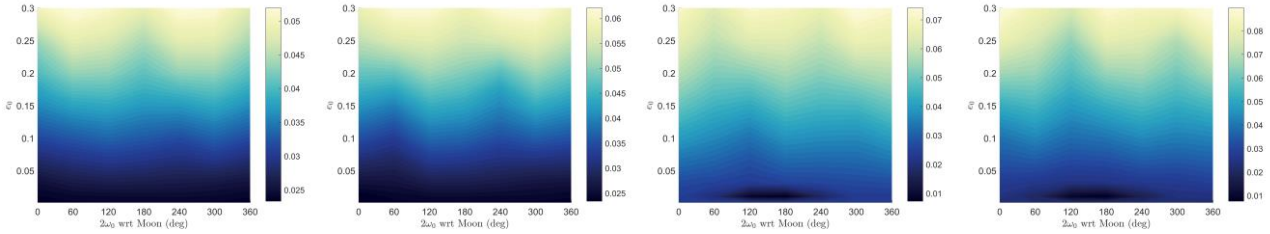

i) i_0=15 deg *l) i_0=20 deg* *m) i_0=25 deg* *n) i_0=30 deg*

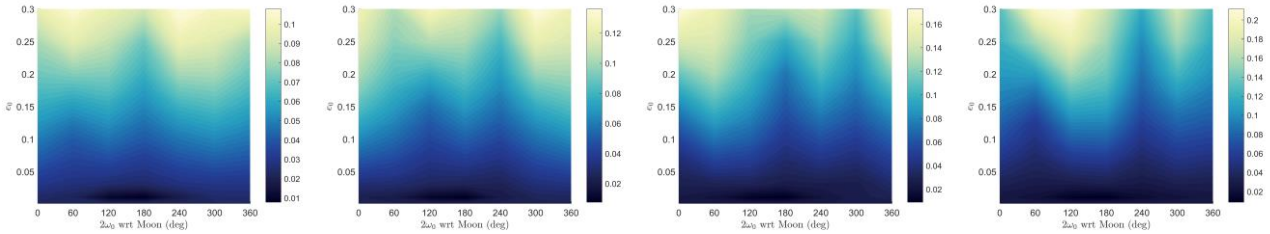

o) i_0=35 deg *p) i_0=40 deg* *q) i_0=45 deg* *r) i_0=50 deg*

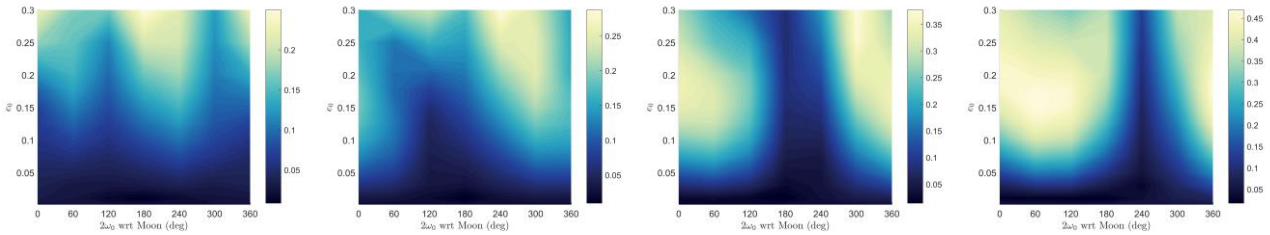

s) i_0=55 deg *t) i_0=60 deg* *u) i_0=65 deg* *v) i_0=70 deg*

Figure 13. Maximum variation Δe over 30 years for initial orbit with $a = r_{\mathrm{GEO}}$, $\Omega_0 = 0$, initial eccentricity between [0−0.3] and inclination of inclination range of [0 − 70] deg, satellite with $c_R\, A/m = 1$ m²/kg.

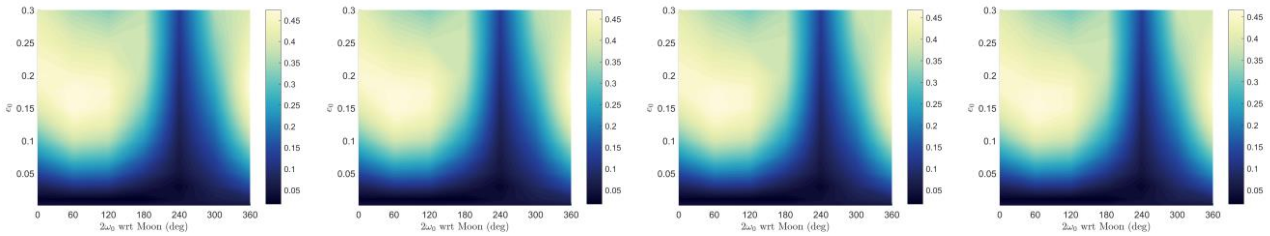

s) i_0=70 deg, Δa=−500 km *t) i_0=70 deg, Δa=−200 km* *u) i_0=70 deg, Δa=250 km* *v) i_0=70 deg, Δa=500 km*

Figure 14. Maximum variation Δe over 30 years for initial orbit with i_0=70 deg, $\Omega_0 = 0$, initial eccentricity between [0−0.3], semi-major axis around the GEO region, satellite with $c_R\, A/m = 1$ m²/kg.

6 CONCLUSION

The dynamics of the geostationary orbit shows dynamical behaviours influenced by the Earth's triaxiality, through the resonant longitude angle, by the luni-solar perturbation through long term oscillation in eccentricity, anomaly of the perigee, inclination and right ascension of the ascending node. For low initial inclinations, as expected, no re-entry conditions are found around the geostationary orbit region; for this reason it is useful in this analysis to study the total variation of eccentricity cover during the long-term propagation, as this can be used as a measure of the stability of the orbit, for choosing, e.g., an appropriate graveyard orbit. For higher initial inclination and low eccentricity conditions the Lidov-Kozai mechanics is present also in this orbit regime. This can be seen by the eccentricity-perigee plot, where the anomaly of the perigee is represented with respect to the Earth-Moon plane. At starting inclinations above 55 degrees, re-entry via natural eccentricity growth is possible with a time span of around 120 years. This analysis will form the basis for the disposal manoeuvres in the next phase of this work.

7 ACKNOWLEDGMENTS

The research leading to these results has received funding from the Horizon 2020 Program of the European Union's Framework Programme for Research and Innovation (H2020-PROTEC-2015) under REA grant agreement number 687500 – ReDSHIFT. The authors would like to thank the Institute of Space Systems, Technische Universitaet Braunschweig for providing the MASTER 2013 debris population. We thank the member of the IFAC-CNR (A. Rossi, E. M. Alessi, G. Schettino, G. B. Valsecchi) and the Thessaloniki team (K. Tsiganis, D. K. Skoulidou, A. J. Rosengren, D.) for the collaboration on Work Package 3.

REFERENCES

1. ESA, "Requirements on Space Debris Mitigation for ESA Projects.
2. Chobotov, V. A., (1990). Disposal of Spacecraft at End of Life in Geosynchronous Orbit. In *Journal of Spacecraft and Rockets*, Vol. 27. No. 4, pp. 433-437.
3. Chao, C. G., Geosynchronous Disposal Orbit Stability. In *American Institute of Aeronautics and Astronautics*, Report AIAA-98-4186.
4. Wytrzyszczak I., Breiter S., (2001). Long-term evolution of disposal orbits beyond the geostationary ring In *Advances in Space Research*, Vol. 28, No. 9, pp. 1409-1414.
5. Lewis H. G., Swinerd G. G., Martin C. E., Campbell W. S., (2004). The Stability of Disposal Orbits at Super-Synchronous Altitudes. In *Acta Astronautica*, Vol. 55, No. 3–9, pp. 299-310. doi: http://doi.org/10.1016/j.actaastro.2004.05.022.
6. Chao C.C. (George), Campbell S., (2005). Long-term perigee height variations of GEO disposal orbits - A revisit. In *Proceedings of the 4th European Conference on Space Debris* (ESA SP-587), 18-20 April 2005, ESA/ESOC, Darmstadt, Germany.
7. Delong N., Frémeaux C. (2005). Eccentricity Management for Geostationary Satellites during End of Life Operations. *In Proceedings of the 4th European Conference on Space Debris* (ESA SP-587). 18-20 April 2005, ESA/ESOC, Darmstadt, Germany, p. 297
8. Anselmo L. Pardini C., (2008). Space debris mitigation in geosynchronous orbit. In *Advances in Space Research*, Vol. 41, No. 7. doi: 10.1016/j.asr.2006.12.018
9. Friesen L. J., Jackson A. A., Zook H. A., Kessler D. J. (1992). Analysis of orbital perturbations acting on objects in orbits near geosynchronous Earth orbit. In *Journal of Geophysical Research*, Vol. 97, No. E3, pp. 3845 –3863.
10. Johnson N.L., 2012. A new look at the GEO and near-GEO regimes: operations, disposals, and debris. In *Acta Astronautica*. Vol. 80, pp. 82–88.
11. Schildknecht T., Musci R., Ploner M., et al., (2004). Optical observations of space debris in GEO and in highly-eccentric orbits. In *Advances in Space Research*. Vol. 34, pp. 901–911.
12. Valk S., Delsate N., Lemaître A., Carletti T., (2009). Global Dynamics of High Area-to-Mass Ratios GEO Space Debris by Means of the MEGNO Indicator. In *Advances in Space Research*, Vol. 43, No. 10, pp. 1509-1526. doi: http://doi.org/10.1016/j.asr.2009.02.014
13. Rosengren A. J., Scheeres D. J. McMahon J. W., (2014). The Classical Laplace Plane as a Stable Disposal Orbit for Geostationary Satellites. In *Advances in Space Research*, Vol. 53, No. 8, pp. 1219–1228. doi: http://doi.org/10.1016/j.asr.2014.01.034
14. Tang J., Liu L. (2014). Disposal strategy for the geosynchronous orbits of the BeiDou Navigation Satellite System. In *40th COSPAR Scientific Assembly*, 2-10 August 2014, Moscow, Russia, Abstract PEDAS.1-29-14.
15. Tang J., Hou X., Liu, L., (2017). Long-term evolution of the inclined geosynchronous orbit in Beidou Navigation Satellite System. In *Advances in Space Research*, Vol. 59, No. 3, p. 762–774.
16. Alessi E.M., Schettino G., Rossi A., Valsecchi G.B., (2017). LEO Mapping for Passive Dynamical Disposal, In *Proceedings of the 7th European*

Conference on Space Debris, ESA/ESOC, Darmstadt, Germany. 18 - 21 April 2017.

17. Skoulidou D. K., Rosengren A. J., Tsiganis K., Voyatzis G., (2017). Cartographic Study of the MEO Phase Space for Passive Debris Removal, In *Proceedings of the 7th European Conference on Space Debris*, ESA/ESOC, Darmstadt, Germany. 18 - 21 April 2017.

18. Union of Concern Scientists database of active satellite on the 07/01/2016 (satellites currently orbiting Earth).

19. Lücking C., Colombo C., McInnes C. R. (2013). Solar radiation pressure-augmented deorbiting: passive end-of-life disposal from high-altitude orbits. In *Journal of Spacecraft and Rockets*, Vol. 50, pp. 1256–1267.

20. Colombo C. (2015). Long-term evolution of highly-elliptical orbits: luni-solar perturbation effects for stability and re-entry. In *Proceedings of the 25th AAS/AIAA Space Flight Mechanics Meeting*, Williamsburg, Virginia, AAS-15-395.

21. Colombo C. (2016). Planetary orbital dynamics (PlanODyn) suite for long term propagation in perturbed environment. In *Proceedings of the 6th International Conference on Astrodynamics Tools and Techniques (ICATT)*, Darmstadt, Germany.

22. Dormand J. R., Prince P. J., (1980). A Family of Embedded Runge-Kutta Formulae. In *Journal of Computational and Applied Mathematics*, Vol. 6, No. 1, pp. 19–26.

23. Shampine L. F., Reichelt M. W., (1997). The MATLAB ODE Suite. In *SIAM Journal on Scientific Computing*, Vol. 18, 1997, pp. 1–22.

24. Montenbruck O., Gill E., (2000). *Satellite Orbits: Models, Methods, and Applications*. Berlin: Springer-Verlag, 2000.

25. Colombo C., Letizia F., Alessi E. M., Landgraf M. (2014). End-of-Life Earth Re-Entry for Highly Elliptical Orbits: The INTEGRAL Mission. In *Proceedings of the 24th AAS/AIAA Space Flight Mechanics Meeting*, Santa Fe, New Mexico, 2014, AAS 14-325.

26. Alessi E. M., Deleflie F., Rosengren A. J., Rossi A., Valsecchi G. B., Daquin J., Merz, K., (2016). A Numerical Investigation on the Eccentricity Growth of Gnss Disposal Orbits. In *Celestial Mechanics and Dynamical Astronomy*, Vol. 125, No. 1, pp. 71–90. doi: 10.1007/s10569-016-9673-4

27. Kozai, Y., "Secular Perturbations of Asteroids with High Inclination and Eccentricity," Astronomical Journal, Vol. 67, 1962, pp. 591-598. doi: 10.1086/108790

28. Colombo C., Lücking C., McInnes C. R., (2012). Orbital Dynamics of High Area-to-Mass Ratio Spacecraft with J_2 and Solar Radiation Pressure for Novel Earth Observation and Communication Services. In *Acta Astronautica*, Vol. 81, No. 1, pp. 137–150. doi: 10.1016/j.actaastro.2012.07.009.